1-2012

Gaining insight into the physics of dynamic atomic force microscopy in complex environments using the VEDA simulator

Daniel Kiracofe
Birck Nanotechnology Center, Purdue University, drkiraco@purdue.edu

John Melcher
Birck Nanotechnology Center, Purdue University, jmelcher@purdue.edu

Arvind Raman
Birck Nanotechnology Center, Purdue University, raman@purdue.edu

AIP | Review of Scientific Instruments

Gaining insight into the physics of dynamic atomic force microscopy in complex environments using the VEDA simulator

Daniel Kiracofe, John Melcher, and Arvind Raman

Citation: Rev. Sci. Instrum. **83**, 013702 (2012); doi: 10.1063/1.3669638
View online: http://dx.doi.org/10.1063/1.3669638
View Table of Contents: http://rsi.aip.org/resource/1/RSINAK/v83/i1
Published by the AIP Publishing LLC.

Gaining insight into the physics of dynamic atomic force microscopy in complex environments using the VEDA simulator

Daniel Kiracofe, John Melcher, and Arvind Raman
School of Mechanical Engineering and Birck Nanotechnology Center, Purdue University, West Lafayette, Indiana 47907, USA

(Received 12 August 2011; accepted 7 November 2011; published online 5 January 2012)

Dynamic atomic force microscopy (dAFM) continues to grow in popularity among scientists in many different fields, and research on new methods and operating modes continues to expand the resolution, capabilities, and types of samples that can be studied. But many promising increases in capability are accompanied by increases in complexity. Indeed, interpreting modern dAFM data can be challenging, especially on complicated material systems, or in liquid environments where the behavior is often contrary to what is known in air or vacuum environments. Mathematical simulations have proven to be an effective tool in providing physical insight into these non-intuitive systems. In this article we describe recent developments in the VEDA (virtual environment for dynamic AFM) simulator, which is a suite of freely available, open-source simulation tools that are delivered through the cloud computing cyber-infrastructure of nanoHUB (www.nanohub.org). Here we describe three major developments. First, simulations in liquid environments are improved by enhancements in the modeling of cantilever dynamics, excitation methods, and solvation shell forces. Second, VEDA is now able to simulate many new advanced modes of operation (bimodal, phase-modulation, frequency-modulation, etc.). Finally, nineteen different tip-sample models are available to simulate the surface physics of a wide variety different material systems including capillary, specific adhesion, van der Waals, electrostatic, viscoelasticity, and hydration forces. These features are demonstrated through example simulations and validated against experimental data, in order to provide insight into practical problems in dynamic AFM. © *2012 American Institute of Physics*. [doi:10.1063/1.3669638]

I. INTRODUCTION

Dynamic atomic force microscopy (dAFM) has become a ubiquitous tool in many different scientific disciplines for imaging, force measurements, and manipulation at scales from micrometers down to atomic resolution. In the early days of dynamic AFM when samples were typically flat, hard materials in ultra high vacuum, a few simple equations could adequately describe the behavior of an AFM cantilever.[1] As dAFM expanded into new areas, many complexities arose. Interpretation of experimental data required consideration of cantilever dynamics,[2,3] non-linear dynamics,[4,5] and convolution of the geometry of the tip and the sample.[6] It was recognized that proper experimental design was required to minimize forces between tip and sample,[7] that different excitation methods produced different results,[8] that increasing imaging speed required attention to controller design,[9] and that fluid structure interactions influenced cantilever response.[10]

In order to provide insight into these complicated systems, various mathematical simulators have been used. The virtual environment for dynamic AFM (VEDA) (Ref. 11) was introduced in 2008. VEDA allows researchers to gain insight into their experimental results, understand non-linear effects, investigate common artifacts, and perform studies to determine the sensitivity to parameter changes. In this article, we report on VEDA version 2.0, which provides significantly enhanced capabilities enabling more advanced simulations. There are advances in three main areas in this version.

First, an emphasis has been placed on accurate simulation in liquid environments. The dynamics of liquid environment AFM are considerably different than ambient or vacuum environment AFM.[12–14] A significant effort has been placed on making sure that the cantilever dynamics, excitation methods and tip-sample interaction models are accurate and consistent for liquid environment simulation. Several experimental simulation comparisons are shown in this work to validate the simulation predictions.

Second, the suite now includes a complete set of tools for every aspect of AFM spectroscopy and imaging. Whereas the original version was limited to Amplitude Modulation (AM) AFM, the new version includes frequency modulation (FM-AFM) modes and static modes (e.g., F-z curves, contact mode scanning) as well as more advanced AM-AFM modes such as bimodal and multi-frequency methods. The modeling of instrumentation such as lock-in amplifiers is also improved.

Finally, a much larger range of materials can be simulated accurately. Nineteen different tip-sample interaction models are available to describe many conservative and non-conservative interactions in non-contact, intermittent contact, and permanent contact regimes in air, vacuum, and liquids.

The layout of the paper is as follows: First, we will review the modeling used in the simulator, including cantilever dynamics, excitation methods, tip-sample interaction models, controllers and instrumentation. Then, we will discuss a number of examples that show the types of simulations available in VEDA and highlight the advanced capabilities present in this new version.

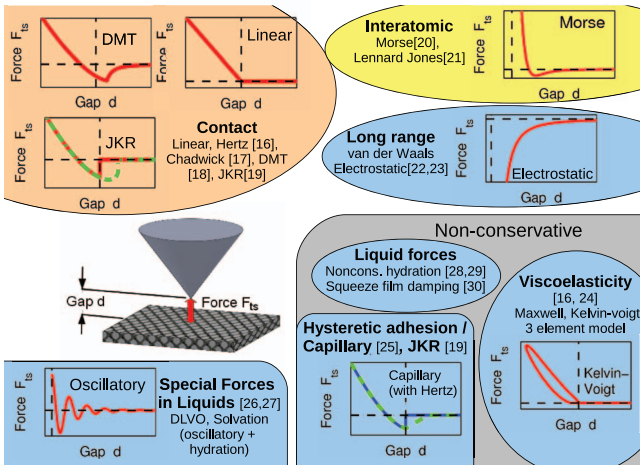

FIG. 1. (Color online) Schematic representation of the different types of tip-sample interaction models available in VEDA. Example plots of tip-sample force versus gap are shown for selected models.

II. MODELING

A. Materials modeling and tip-sample interactions

Various sample materials may present widely differing forces, and these may depend strongly on the environment (e.g., air versus liquid). The set of tip-sample interaction models available in VEDA has been significantly expanded since its original release. Several different categories of models are available as illustrated in Figure 1.

Space does not permit detailed descriptions of all nineteen models. Selected models are given here. Details on the rest are available in the online VEDA manual[15] as well as Refs. 16–30. In particular the implementation of correct viscoelastic Hertzian mechanics including sample relaxation times is also available in VEDA but not described here because validation efforts are ongoing.

1. Hertz contact

The classical Hertz contact theory for a spherical tip indenting a flat plane[31] is

$$F_{ts}(d) = \begin{cases} 0, & d > 0 \\ \frac{4}{3}E^*\sqrt{R}d^{3/2}, & d \le 0, \end{cases} \quad (1)$$

where F_{ts}, d, R are the tip-sample interaction force, tip-sample gap, tip radius, respectively and E^* is the reduced elasticity

$$E^* = \left[\left(1-\nu_{tip}^2\right)/E_{tip} + \left(1-\nu_{sample}^2\right)/E_{sample}\right]^{-1}, \quad (2)$$

where ν and E are Poisson's ratio and Young's modulus of the tip and the sample. For later reference, when the tip becomes rigid ($E_{tip} \to \infty$), then $E^* = E_{sample}/(1-\nu_{sample}^2)$ and (1) could be written in terms of the shear modulus G and Poisson's ratio using the relation $E^* = 2G_{sample}/(1-\nu_{sample})$.

2. DMT contact

The Derjaguin-Muller-Toporov (DMT) theory[18] combines classical Hertz contact with an attractive van der Waals force to model the attractive forces between stiff samples with low adhesion:

$$F_{ts}(d) = \begin{cases} -\frac{HR}{6d^2}, & d > 0 \\ -\frac{HR}{6a_0^2} + \frac{4}{3}E^*\sqrt{R}(a_0-d)^{3/2}, & d \le 0, \end{cases} \quad (3)$$

where H and a_0 are the Hamaker constant and intermolecular distance.

3. JKR contact

The Johnson-Kendall-Roberts (JKR) model[19] applies to highly adhesive, highly compliant surfaces and allows the sample to "neck" in the presence of an adhesive load. The model is nonconservative and includes a dependency of the history of the tip-sample contact. The JKR model can be written compactly through the use of a mode variable m describing the state of the tip-sample contact.[32] Let $m = 1$ signify contact with the sample and $m = 0$ otherwise. Then the force can be expressed as

$$F_{ts}(a,m) = \begin{cases} 0, & m = 0 \\ \frac{4E^*a^3}{3R} - \sqrt{8\pi W_{JKR}E^*a^3}, & m = 1, \end{cases} \quad (4)$$

where $W_{JKR} = 2F_{ad}/3\pi R$ is the work of adhesion, F_{ad} is the adhesion force, a is the contact radius that is described implicitly as

$$d = -\frac{a^2}{R} + \sqrt{\frac{2\pi W_{JKR}a}{E^*}} \quad (5)$$

where the critical gap $d_{crit} = \sqrt{2\pi W_{JKR}a_{crit}/E^*} - a_{crit}^2/R$ is the distance at which the contact terminates, and $a_{crit} = (\pi Rtip^2 W_{JKR}/8E^*)^{1/3}$ is the contact radius at which $d = d_{crit}$. While approaching in noncontact ($m = 0$), contact occurs at $d = 0$ where the mode variable changes to $m = 1$. Upon retraction from the sample, tip-sample contact persists until $d > d_{crit}$. At this point, the tip and sample separate and the mode changes to $m = 0$.

Hysteretic models such as JKR (and the hysteretic adhesion model in Sec. II A 7) present some difficulties when used with adaptive-step, backwards differentiation ODE solvers such as that used in VEDA (DDASKR (Ref. 33)). Such solvers may compute intermediate trial solution that are then discarded (e.g., finite difference approximations to the Jacobian matrix or iterative solution methods for ODE). All of these trial solutions involve evaluation of F_{ts}. Therefore, the routine that evaluates the hysteretic adhesion force must ensure that when $0 < d < d_{crit}$, m retains its value from most recently computed actual solution point, not the most recently computed intermediate point.

4. Hydration forces

There are several types of short ranges forces that occur within a few molecular diameters of a solid surface. In this work, we focus on the "hydration" force, which is so named

because it may be linked to the energy required to remove hydrated water molecules from the surface. Some authors also refer to this force as a solvation force[27] because it may be caused by solvent molecules. The origins of this force, which is at present not fully understood, is discussed in Ref. 26. Between hydrophillic surfaces, this force is repulsive. The conservative part of this force can be modeled as an exponentially decaying force[27,28]

$$F_{ts}(d) = 2\pi R^2 p_h \exp\left(-\frac{d}{\lambda}\right),$$

where R is the tip radius and λ and p_h are empirically determined decay lengths and scalings.

In addition to conservative forces, it has been recognized that there are also dissipative (non-conservative) components to the hydration/solvation forces. There is still debate in the literature as to the exact form of these forces. Some authors propose that the dissipation is oscillatory (proportional to the stiffness terms),[28] whereas other claim that the dissipation is monotonic and oscillatory components are instrumental artifacts.[29] One simple model is treat the force as a viscous drag where the viscosity decays exponentially away from the wall, and the force is zero when the tip and sample are in contact:

$$F_{ts}(d,\dot{d}) = \begin{cases} ce^{-\frac{d}{\sigma}}\dot{d}, & d > 0 \\ 0, & d < 0, \end{cases} \tag{6}$$

where c is a scaling (kg/s) and σ is a decay length (typically the molecular diameter). However, this causes the force to be discontinuous at the wall (i.e., $F_{ts}(0^+,\dot{d}) = c\dot{d}$ but $F_{ts}(0^-,\dot{d}) = 0$). Discontinuous forces can cause non-physical high frequency cantilever response. Therefore, we smooth the force out by allowing it to decay smoothly to zero as the tip indents the sample:

$$F_{ts}(d,\dot{d}) = \begin{cases} ce^{-\frac{d}{\sigma}}\dot{d}, & d > 0 \\ ce^{\frac{d}{\sigma/3}}\dot{d}, & d < 0. \end{cases} \tag{7}$$

We will show in Sec. IV that this simple model is sufficient to capture the behavior of water over mica.

5. Morse potential

The Morse potential is commonly used to describe interatomic forces. It is often used in non-contact FM-AFM to describe the short range forces between the atoms on the tip and atoms on the sample. Van der Waals forces may be added to describe the long range forces between the atoms in the bulk of the tip and the bulk of the sample (e.g., Ref. 34). The force is given by:

$$F_{LJ}(d) = -\frac{HR}{6d^2} + \frac{2U_0}{\lambda}\left[\exp\left(\frac{r_c - d}{\lambda}\right) - \exp\left(\frac{2r_c - 2d}{\lambda}\right)\right],$$

where H is the Hamaker constant, R is the tip radius, U_0 is the depth, r_c is the equilibrium distance, and λ is the range.

6. Electrostatic force

VEDA allows the use of two different electrostatic models. The first is the simple model of Ref. 22 for the long range electrostatic force between a sphere and a plane:

$$F(d) = -4\pi\varepsilon_0 \frac{\varepsilon - 1}{\varepsilon + 1}\frac{R^2}{d^2}V^2, \tag{8}$$

ε_0, ε, and R are the permittivity of free space, relative dielectric constant, and tip radius and V is the potential difference between the tip and sample $V = V_{DC} - \phi_{surface} + V_{AC}\cos(\omega_{AC}t)$ where V_{DC}, $\phi_{surface}$, V_{AC}, ω_{AC} are the applied DC bias voltage, surface potential, applied AC bias voltage, and bias frequency, respectively.

VEDA also includes the more complex model of Ref. 23, which splits the AFM probe up into three parts: the main body of the cantilever, the bulk of the tip (modeled as a truncated cone), and the apex of the tip (modeled as a paraboloid). The electrostatic force contributions from each component are accounted for separately,

$$F_{total}(d) = \frac{4\pi}{(\pi - \theta_{lever})^2}\varepsilon\varepsilon_0\left(ln\left(\frac{d - \frac{\delta}{2} + h}{d + \frac{\delta}{2}}\right) - sin\left(\frac{\theta_{tip}}{2}\right)\frac{h - \delta}{\left(d - \frac{\delta}{2} + h\right)}\frac{d - \frac{\delta}{2}}{d + \frac{\delta}{2}}\right)V^2 - \frac{HR}{6d^2}, \tag{9}$$

where l, w, θ_{lever}, h, and θ_{tip} cantilever length, cantilever width, cantilever inclination angle (with respect to the sample surface), tip height, tip opening angle, and tip apex radius, respectively, $\delta = R/\tan^2(\theta_{tip}/2)$ is the height of the truncated part of the cone, and the final term is the van der Waals force on the tip (same form as in previous models).

7. Hysteretic adhesion / capillary forces

Apart from JKR contact, there are many situations in AFM that involve hysteretic adhesion (i.e., a different attractive force when the tip is retracting from the surface than when it approaches). A common example is capillary forces: When a tip comes into contact with a sample in the presence of moist air, a liquid capillary neck can form between them. When the tip retracts, the capillary neck breaks. This process causes a hysteretic, non-conservative force. Another example is specific chemical interactions between a functionalized tip and a sample,[35,36] which is commonly used in biological studies in liquid environments.

An *ad hoc* model intended to capture hysteresis in the tip-sample adhesion is taken from Ref. 25. The hysteretic force in this model can be added to any of the other contact models listed in Figure 1. The force is given by

$$F_{ts}(d,m) = \begin{cases} 0, & m = 0 \\ \frac{2\Delta E}{D_{crit}^2}(d - D_{crit}), & d \geq d_0, m = 1 \\ F_{ad,cap}, & d < d_0, m = 1, \end{cases} \tag{10}$$

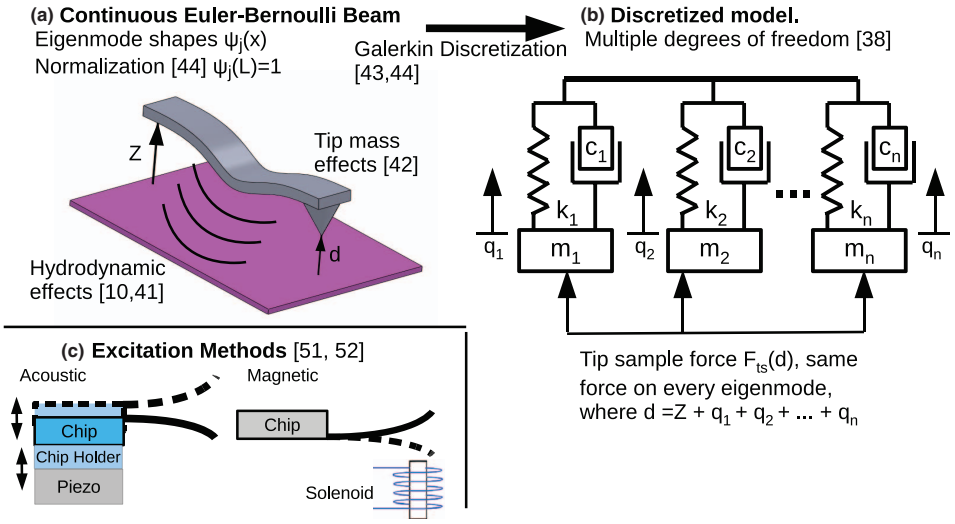

FIG. 2. (Color online) A graphical representation of the key issues in modeling cantilever dynamics. The cantilever (a) is a continuous structure, thus the dynamics are governed by a partial differential equation (PDE). Simply replacing it by a point-mass oscillator does not correct capture the dynamics. Instead a Galerkin discretization converts the PDE into a series of ordinary differential equations, each representing one eigenmode of the continuous beam. Each degree of freedom in the discretized model (b) is independent of the others, except for the coupling through the tip-sample interaction force. Additional considerations are: the eigenmode must be normalized such the tip deflection is unity (Ref. 44), a large massive tip can change the higher eigenmode shapes, stiffnesses, and sensitivities (Ref. 42) and quality factor and natural frequency are both affected by interaction with the surrounding fluid (Ref. 41). Finally, different excitation methods lead to significantly different modeling (c) (Refs. 51 and 52).

where $d = d_0$ is the distance at which the neck forms (for the DMT model, $d_0 = a_0$ the intermolecular distance, for all other models $d_0 = 0$), $d = D_{crit}$ is the distance at which the neck breaks, ΔE is the energy dissipated per hysteretic cycle, $F_{ad,\,cap}$ is the force jump when the capillary neck forms $F_{ad,cap} = 2\Delta E/D_{crit}^2(d_0 - D_{crit})$ and m is a state variable defined as follows: When $d \geq D_{crit}$, then m is set to 0 and the capillary neck is "off". When $d \leq a_0$, then m is set to 1 and the capillary neck is "on". When $d_0 < d < D_{crit}$ then m retains its value from the previously computed point (i.e., 0 when approaching and 1 when retracting). See Figure 1 for an example graph.

B. Cantilever dynamics

In order to simulate the AFM probe's interaction with samples, it is important to model the cantilever dynamics accurately. There are several key details which must be addressed in this modeling. These are summarized graphically in Figure 2 and we discuss the details in this section.

Dynamic AFM is often modeled assuming that the cantilever probe could be treated as a single degree of freedom oscillator. This assumption, which is generally valid for classical single frequency operation in ambient or ultra-high vacuum environments,[37] was used in the original version of VEDA. However, operation in liquids,[38] as well as new advanced multi-frequency techniques (e.g., Refs. 39 and 40) necessitate high-fidelity probe dynamics that capture multiple eigenmodes of the continuous microcantilever probe. Accordingly, VEDA 2.0 allows multiple eigenmodes to be simulated.

Here we show the equations of motion that VEDA uses. The derivation is similar to Ref. 11, only the number of eigenmodes is changed. Specifically, we start from the classical Euler-Bernoulli beam partial differential equation for small deflections of a slender, rectangular cantilever in a ground-fixed inertial frame, subject to a hydrodynamic damping force, a driving force, and a tip-sample interaction force,

$$EI\frac{\partial^4 w(x,t)}{\partial x^4} + \rho_c A\frac{\partial^2 w(x,t)}{\partial t^2} = F_{hydro}(w) + F_{drive}(x,t) + F_{ts}(w(L,t)+Z)\delta(x-L), \tag{11}$$

where E, I, ρ_c, A, w, x, t, F_{hydro}, F_{ts}, F_{drive}, L, Z and δ are the cantilever Young's modulus, area moment of inertia, density, cross-sectional area, deflection, axial coordinate, time, hydrodynamic force,[10,41] tip-sample interaction force, driving (excitation force), cantilever length, cantilever-sample separation and Dirac delta, respectively. The hydrodynamic forces are converted into an effective modal viscosity and modal added mass,[42] and then the equation is discretized in the basis of cantilever eigenmodes using Galerkin's method[43] following Ref. 44. The method is to write w as $w = \sum_{i=1}^{\infty} q_i(t)\psi_i(x)$ where $\psi_i(x)$ is the ith eigenmode shape and $q_i(t)$ is referred to as a modal coordinate. If ψ is chosen such that $\psi_i(L) = 1$, then the modal coordinates are the deflection of cantilever at the free end. This scaling is important because it allows the calibrated stiffnesses of the eigenmodes to be incorporated directly into the model.[44] An approximation is made by keeping only the first N eigenmodes and neglecting the rest (typically N = 1 in air or vacuum and N = 2 or 3 in liquid, although VEDA allows up to N = 9). After a series of manipulations, the original partial differential equation is reduced to a set of ordinary differential equations:

$$\frac{\ddot{q}_i}{\omega_i^2} + \frac{\dot{q}_i}{\omega_i Q_i} + q_i = \frac{F_{ts}(d)}{k_i} + \frac{F_i \cos\Omega_d t}{k_i}, \quad i = 1 \ldots N, \tag{12}$$

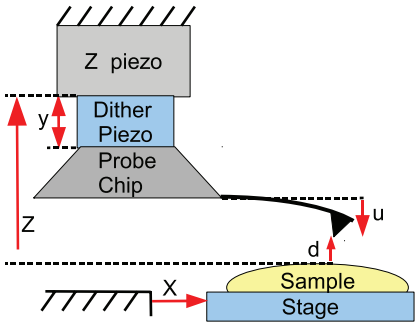

FIG. 3. (Color online) Schematic of a typical AFM showing the coordinates used in modeling.

where $q_i(t)$, ω_i, Q_i, k_i, F_{ts}, and F_i are the tip deflection, natural frequency, quality factor, equivalent stiffness, tip-sample interaction force, and driving force of the *ith* eigenmode, respectively, $d = Z + \sum_{i=1}^{N} q_i$ is the tip-sample gap. Ω_d is the driving frequency, which may be different than ω_j in order to explore off-resonant dynamics. The coordinates used in these formulas are defined graphically in Figure 3.

Finally, to model the optical beam deflection method,[45] which measures slopes not actual deflections, observed deflection is reported as

$$\tilde{u} = \sum_{i=1}^{N} \frac{\chi_i}{\chi_1} q_i, \tag{13}$$

where χ_i is slope at the end of the *i*th eigenmode. This assumes the photodiode volts-to-nanometers conversion has been calibrated for the 1st eigenmode. In typical experiment conditions, the photodiode may be calibrated from an F-z curve on a stiff surface. This gives the static bending sensitivity χ_s. For a rectangular Euler-Bernoulli beam, the static sensitivity is related to the first eigenmode sensitivity by,[46] $\chi_1 = 0.917\chi_s$. An alternative is the method of Ref. 47, which can give χ_1 directly. Direct measurement of χ_i for $i \geq 2$ is difficult and the authors are not aware of any commonly used method. Typically, the theoretical values of χ_i/χ_1 from Euler-Bernoulli beam theory are used.

While the development above focused on rectangular cantilevers, the resulting discretized equations are similar when using cantilevers of any other geometry such as triangular levers. The main difference is that the modal stiffnesses follow a different pattern. For example $k_2/k_1 = 40$ for a rectangular beam but k_2/k_1 may be 17 for triangular cantilevers, depending on the exact geometry.[44] Also anti-symmetric eigenmodes of triangular cantilevers cause only a torsional deflection of the tip and no normal deflection.[48,49] Because VEDA is not able to model torsional deflections, these eigenmodes cannot be simulated.

For convenience, many quantities of the higher eigenmodes such as stiffness, natural frequency, and slope χ can be automatically calculated from Euler-Bernoulli theory based on the values of the first eigenmode. All of these parameters can be affected significantly by the mass of the tip,[42] and VEDA is able to take that effect into account.

VEDA solves these dynamic equations even for static modes such as contact mode or F-z curves. When operated at sufficiently high speeds, the topography of the sample acts as a dynamic excitation and the cantilever dynamics become relevant to understanding the response.[50]

C. Excitation methods

In air or vacuum, the choice of excitation method is usually not critical. In liquid environments, and especially for frequency modulation, the choice of excitation method makes a large difference to the final result. Common excitation methods include acoustic (mechanically shaking the base of the cantilever with a dither piezo), magnetic (coating the cantilever with a magnetic material and generating an alternating magnetic field with a solenoid), and Lorentz force (depositing a conducting loop of metal on the cantilever and running an AC current through it in the presence of a steady magnetic field). The models for these excitation types can be derived from the equations given in Ref. 51.

For magnetic drive or Lorentz force, the driving force is assumed to be uniform along the width of the cantilever. Therefore,

$$F_i = F_{mag} \frac{1}{L} \int_0^L \psi_i(x) dx, \tag{14}$$

For acoustic drive, the situation is significantly more complicated. A complete derivation is given in Ref. 52, which is summarized here briefly. The tip-sample gap is now described by $d = Z + y(t) + \sum_{i=1}^{N} q_i$, where $y(t)$ is the motion of the cantilever base due to dither piezo excitation and the q_i are the tip deflection relative to base motion (i.e., in the moving frame[51]). The moving boundary condition at the base is converted into an equivalent modal forcing. In liquids, an additional fluid borne loading force may be added to account for direct excitation from unsteady fluid motion excited by the dither piezo.[51,52] The total force takes this form:

$$F_j(\omega) = Y(\omega) \left\{ \frac{\beta_j + \bar{m}}{\alpha_j + \bar{m}} \omega^2 - i \frac{\beta_j}{\alpha_j} \frac{\omega_j}{Q_j} \omega + \left(\frac{\beta_j}{(\alpha_j + \bar{m})} \times \frac{m^*}{(m_c + m^*)} \omega^2 - \omega i \frac{\beta_j}{\alpha_j} \frac{\omega_j}{Q_j} \right) A_{fluid}(\omega) \right\}, \tag{15}$$

where $m_c = \rho_c AL$ is the cantilever mass, m^* is the hydrodynamic added fluid mass, and $\bar{m} = m_{tip}/(m_c + m^*)$ is the ratio of tip mass to total cantilever plus added fluid mass, $\beta_j = (1/L)\int_0^L \psi_j(x)dx$, $\alpha_j = (1/L)\int_0^L \psi_j^2(x)dx$, $\psi_j(x)$ is the *j*th eigenmode shape, $Y(\omega)$ is the Fourier transform of the base motion, and A_{fluid} describes the ratio of fluid borne loading to structural borne loading.

In air, the effect of fluid borne loading is negligible, so this expression reduces to

$$F_{j,air}(\omega) = Y(\omega) \left\{ \frac{\beta_j + \bar{m}}{\alpha_j + \bar{m}} \omega^2 - i \frac{\beta_j}{\alpha_j} \frac{\omega_j}{Q_j} \omega \right\}, \tag{16}$$

and in liquids, the hydrodynamic added mass m^* is typically large, such that $\bar{m} \ll 1$ and $m^*/(m_c + m^*) \approx 1$:

$$F_{j,liquid}(\omega) = Y(\omega) \frac{\beta_j}{\alpha_j} \left(\omega^2 - i \frac{\omega_j}{Q_j} \omega \right) (1 + A_{fluid}). \tag{17}$$

Multiple frequency excitations are also possible, for example bimodal AFM.[39] Bimodal excitation will be discussed in Sec. IV E.

D. Controllers and instrumentation modeling

Having described a complete set of models for cantilever dynamics and tip-sample interaction forces, one more set of models is needed to simulate a real instrument: controllers and instrumentation. Example block diagrams of the complete system are shown in Figure 4.

The original release of VEDA included only Amplitude Modulation tools, but this release now includes Frequency Modulation tools.[53] The implementation uses a PLL (Phased-locked loop) for maintaining constant phase, as opposed to a self-excited loop, and a standard feedback controller for maintaining constant amplitude as shown in Figure 4. Both the PLL and amplitude controller use PID feedback, which affords better response than the PI control used by some FM AFMs. The method of Ref. 54 is used to automatically set feedback parameters, which greatly speeds up the simulation process. Also, for operation in liquids (and especially with acoustic drive) the phase lag setpoint is not necessarily 90 degrees. FM-AFM results can be misleading when an incorrect phase setpoint is used.[29] The correct setpoint is calculated automatically from the cantilever dynamics models in II B.

Particular care must be paid to the excitation modeling when FM is used, as the excitation force may change at different frequencies. To consider a simple example, when using magnetic excitation, the impedance of the exciting solenoid coil increases as frequency increases.[55] Thus the magnetic force will drop slightly as frequency increases. This will cause the amplitude controller to increase the driving voltage to compensate. The increased driving signal will look like an apparent dissipation.

In liquids with acoustic excitation, the situation can be significantly more complicated. The presence of dither piezo resonances may cause the excitation force to change significantly as the driving frequency is changed. This can cause artifacts in the frequency shift and drive signal ("dissipation") outputs.[56,57] VEDA is able to simulate dither piezo resonances and thus accurately reproduce these artifacts. For example, in Equation (17), $Y(\omega)$ can be modeled as a simple harmonic oscillator

$$Y(\omega) \propto \frac{1}{\omega_{piezo}^2 + i\frac{\omega\omega_{piezo}}{Q_{piezo}} - \omega^2},$$

where Q_{piezo}, ω_{piezo} are the quality factor and natural frequency of the dither piezo resonance. Then, as the PLL changes the driving frequency, the cantilever base motion changes accordingly.

The dynamics of the X, Y, and Z piezos, however, are neglected. That is, the X,Y, and Z piezos are assumed to respond instantaneously to a controller command. No X, Y, or Z piezo resonances, hysteresis, creep, or non-linearities are included.

The original release of VEDA used Fourier integrals over a specified number of drive cycles as an approximation to a lock-in amplifier. The current version include a complete model of a lock-in amplifier with choice of 1st, 2nd, or 4th order filtering and adjustable time constants. This allows simulation of the effects of lock-in amplifier choice on speed of response, noise rejection, and controller performance. Up to ten different lock-ins can be used simultaneously in order to extract higher harmonics information and model advanced modes of operation.

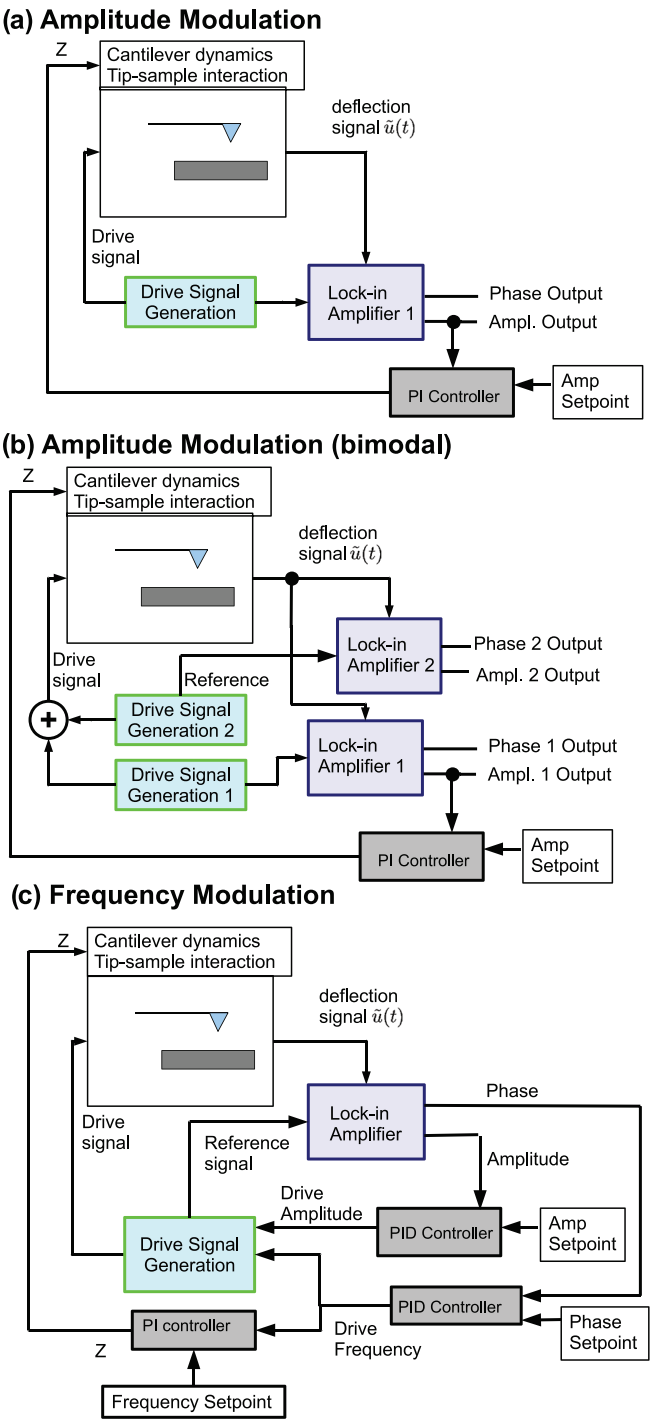

FIG. 4. (Color online) Example block diagrams of the VEDA simulator for common configurations. (a) Amplitude-modulated scanning, (b) bimodal amplitude-modulated scanning, and (c) frequency-modulated scanning.

VEDA reports phase using a phase lag convention (i.e., phase increases from 0 to + 180 degrees when excitation frequency is swept up through resonance).

E. Comparison to other simulators

It is worth comparing and contrasting the modeling assumptions in VEDA with other simulators.

First, VEDA solves the differential equations of motion directly in time domain, as opposed to methods that use approximate equations derived using asymptotic/perturbation ("averaging") techniques.[58] This means that VEDA is somewhat slower than those solvers, but it is possible to simulate complex dynamics and interaction models for which perturbation methods do not work. For example, as we will discuss in Secs. IV A and IV F liquid simulations generally involve low quality factors, multiple eigenmodes, and multiple harmonics, which pose difficulties for typical perturbation methods. Further, VEDA incorporates several discontinuous interaction models such as hysteric adhesion and JKR contact that cannot be treated by standard perturbation methods.

VEDA is a general simulator, able to handle a wide variety of imaging modes, environments and samples. The control system architecture is fairly generic. In contrast, many existing simulators are more specialized. For example, some are focused solely on FM-AFM,[59,60] while others have tried to exactly match one particular instrument.[61]

VEDA uses a modal discretization of the cantilever (details in Sec. II B) whereas some solvers have used a finite-difference[62] or finite-element discretization.[63] For uniform rectangular cantilevers a modal discretization is significantly faster than a finite-element/finite-difference approach with no loss in accuracy. On the other hand, the finite-element method is better equipped to handle highly non-uniform or irregular geometry.

Finally, the focus in VEDA has been on correctly modeling dynamics and interactions. Some simulators have focused on generating 2D images based on the convolution of three dimensional tip and sample geometries (or force fields) with either no or simplified cantilever dynamics.[58,64] While VEDA does include scanning simulations, it only simulates one line at a time and is limited to simpler geometry.

III. DESCRIPTION OF TOOLS

The VEDA suite currently includes 11 tools. These can be classified in several different ways

- *Operating mode*: contact, amplitude modulation, frequency modulation.[65]
- *Experiment type*: approach curves, scanning, frequency sweep.
- *Basic versus advanced*. Because the number of inputs on the various tools can be daunting to a new user, basic versions of some tools are provided as easier to learn alternative. The basic versions are applicable to air or vacuum environments only.

The basic AM approach curves and basic AM scanning tools correspond to the tools available in the original release of VEDA and the other nine tools represent new functionality.

A. Web-based graphical user interface

A key feature in VEDA is that the graphical user interface (GUI) is entirely web-based (using the rappture[66] toolkit). This allows simulations to be run from any location with a Java-based web browser. Users do not need to install any software on their local machine. The actual computations are run on the nanoHub cloud, so computationally intensive simulations can be run even if the researcher is not using a high-powered, expensive workstation.

Each of the different tools has a different interface that asks for the inputs relevant to that simulation. Inputs that are common to multiple different tools (such as tip-sample interaction models) are grouped together.

The GUI includes a plotting package for post-processing, and it is possible to plot multiple simulations on top of each other. This makes it easy to perform parameter studies. Results can also be downloaded as CSV files for plotting in the user's preferred graphics package.

B. Pedagogical features

VEDA has been used as an integral part of a semester long class on the fundamentals of atomic force microscopy (complete lectures are freely available online at Ref. 67). In order to assist students' learning, VEDA comes with a number of example simulations that can be accessed from drop-down menus. These simulations illustrate various points of dAFM, and are described in detail in the accompanying manual. The manual also gives additional descriptions of the basic theory and operation of dAFM, making it suitable as a supplementary textbook for classes.

C. Open source

In addition to the web-based GUI, the complete FORTRAN 90 source code is also available for download. Users may compile and run VEDA on any machine on which the rappture toolkit is supported (currently Linux and Mac).

IV. EXAMPLE SIMULATIONS

In this section, a number of example simulations are presented. A wide variety of cases are shown in order to demonstrate the new capabilities. All of the simulation examples have been validated against either experimental data or other simulation data, either presented in this paper or previously published. A summary of the validations for each example is given in Table I. The specific examples have been chosen in order to demonstrate the three key types of new features in VEDA

TABLE I. Summary of the validation for each of the examples.

Example	Validation
A (Tapping mode approach curves on mica in deionized water)	Experimental data presented in this work
B (Non-linear Frequency Response in Air)	Ref. 5
C (FM Force Spectroscopy in Vacuum)	Ref. 60
D (Electrostatic Force Spectroscopy)	Qualitative comparison to Refs. 23 and 78
E (Material Contrast in Bimodal Scanning)	Ref. 81
F (Subharmonic Response when Operating at Higher Eigenmodes)	Ref. 82
G (Scanning Artifacts)	Experimental data presented in this work

- *Accurate modeling of cantilever dynamics*
  - Tapping mode approach curves on mica in deionized water (Sec. IV A)
  - Subharmonic response when operating at higher eigenmodes in liquids (Sec. IV F)
- *New operating modes, instrumentation, and controllers*
  - Non-linear frequency response in air (Sec. IV B)
  - Frequency modulation force spectroscopy in vacuum (Sec. IV C)
  - Material contrast in bimodal scanning (Sec. IV E)
- *Enhanced materials modeling*
  - Tapping mode approach curves on mica in deionized water (Sec. IV A)
  - Higher eigenmode enhancement in electrostatic force microscopy (Sec. IV D)

Tables of parameters are listed for each simulation. To save space, some default parameters are not repeated on every table. Unless otherwise specified, all simulations use a tip radius of 10 nm, tip Young's modulus of 130 GPa, Poisson's ratio of 0.3, a 2nd order lock-in, and 1000 points are computed per drive cycle.

A. Tapping mode approach curves on mica in deionized water

This example shows one of the easiest liquid environment AFM experiments to conduct, yet one of the most difficult to simulate accurately. A CSC37 cantilever (Mikromasch) that has been coated with a magnetic material (Agilent) is oscillated with magnetic excitation and approached to a freshly cleaved mica surface in deionized water. The experiments are conducted on an Agilent 5500 AFM with a magnetic coil located below the sample. Experimental parameters are listed in Table II. The experimental results are plotted in Figure 5(a) as first harmonic phase versus setpoint ratio (this removes any cantilever-sample Z drift or Z piezo non-linearity from the measurement) and are the average of five curves. The experiments were replicated with a different cantilever on a different day and result was repeatable.

For the simulation, the tip-sample interaction model has three components: DMT contact, conservative hydration forces, and non-conservative hydration forces. As the media is deionized water, the Debye length is long, so the DLVO theory[27] would predict a nearly constant electrostatic double layer force near the surface. A constant force does not affect the dynamic response therefore the double layer forces are neglected. The conservative hydration force is repulsive and partially cancels out the attractive forces in the non-contact region of the DMT forces. As the oscillation amplitude is large compared to the diameter of a water molecule, contributions from oscillatory forces are expected to average out, so they are neglected. Finally, the non-conservative hydration forces are assumed to be a simple exponentially decaying damping coefficient. The parameters used in the simulations are listed

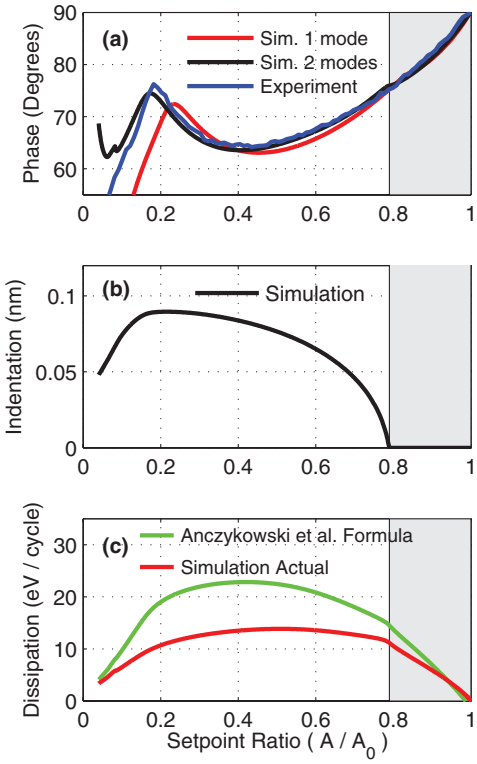

FIG. 5. (Color online) (a) Comparison between experiment and simulation for a soft cantilever approaching a mica surface in deionized water using magnetic drive. The phase (lag) has been shifted to be exactly 90 degrees when the cantilever is not in contact with the sample. A simulation with a two eigenmode model matches the data much better than a 1 eigenmode model. (b) Simulation Indentation. In the shaded region (0.79 to 1.0), the indentation is zero, indicating that the cantilever is being entirely detuned by the solvation shell forces and is not actually touching the sample. In this region the imaging resolution will be poor. (c) Simulation tip-sample energy dissipation. The standard formulas from 1st harmonic amplitude and phase (Ref. 69) significantly over predict the actual value due to energy transferred to higher harmonics/eigenmodes.

TABLE II. Parameters used for the simulation in Figures 5–7 (approach curves on mica in liquid).

Parameter	Value, Figs. 5 and 6	Value, Fig. 7	Source
Simulation	AM Approach Curves		
Natural frequency (kHz)	10.8, 81		Measured in Exp.
Quality factor	2.9, 4.0		Measured in Exp.
Cantilever stiffness (N/m)	0.7		Measured in Exp.
Unconstrained amplitude (nm)	5.4		Measured in Exp.
Drive frequency (kHz)	10.5		Measured in Exp.
van der Waals adhesion force (nN)	1.7		Measured in F-z curves
Hamaker constant (J)	3.4e-20		83
Young's modulus of sample	60		Typical for mica
Hydration force decay length (nm)	0.245	N/A	28
Hydration force scaling	5e6	0	Fit to match experiment
Noncons. hydration force decay length (nm)	0.245	N/A	28
Noncons. hydration force scaling (kg/s)	3.8e-5	0	Fit to match experiment

in Table II. Importantly, all of the parameters are either measured directly during the experiment or taken from the literature, except the scaling of the hydration force has been tuned to match the experimental data.

In comparing the simulation to the experiment, we note that the match is quite good when using a two eigenmode model but not as good when using a one eigenmode model.[38] Because the experimental observables match the simulation, we can then use the simulations to investigate quantities that are not observable during the experiment. For example, Figure 5(b) shows the indentation into the mica surface. Importantly, this is zero between 100% and 80% amplitude ratio. This indicates that above 80% amplitude ratio, the amplitude reduction is coming entirely from the hydration forces and is not actually touching the sample surface. As several groups have suggested,[12,68] the best imaging resolution will be achieved when the tip pushes all the way through the hydration layers and touches the surface atoms. So in this case the best imaging resolution is expected to be at 80% setpoint or below.

Another quantity of interest is the tip-sample energy dissipation. In this case, a large source of dissipation is expected to be within the hydration shells. In tapping mode, experimental energy dissipation is typically calculated from the first harmonic amplitude and phase by means of standard formulas.[69] In the simulation, the tip-sample force and tip velocity are directly accessible, so the actual dissipation can be calculated directly from numerical integration. It can be seen in Figure 5(c) that the standard formula over predicts the tip-sample energy dissipation by more than 60%.

To understand the source of this discrepancy, we examine the time history of tip sample interaction for this simulation at a setpoint ratio of 70%. The time history of tip-sample force and observed deflection are shown in Figure 6(a). When the tip taps on the sample, there is a distortion of the deflection waveform, which would otherwise be sinusoidal. To further investigate, we can directly plot the response of the two different eigenmodes in Figure 6(b). When the tip taps on the sample, there is a spike in the response of the second eigenmode, indicating that a significant amount of energy has been transferred to the second eigenmode. As the tip leaves contact with the sample surface, the second eigenmode rings down–dissipating its energy into the surrounding fluid.

This effect, which we call "momentary excitation" has a significant effect on the dynamics of liquid environment AFM.[12–14,38,70] Indeed, this is the reason why two eigenmode models match experimental data better than one eigenmode models (Figure 5(a)). The energy transfer to higher eigenmodes/higher frequencies explains the difference between the two curves in Figure 5(c). The formula of Ref. 69 represents the total energy lost from the driving harmonic, which actually has two components. One component is tip-sample dissipation and the other component is energy transferred to higher frequencies.

One final point of interest in these results is large peak in the phase at 16% setpoint. Based on Ref. 13, it appears that this might be a point where the tip transitions to a multiple impact regime (i.e., begins to tap on the sample two or

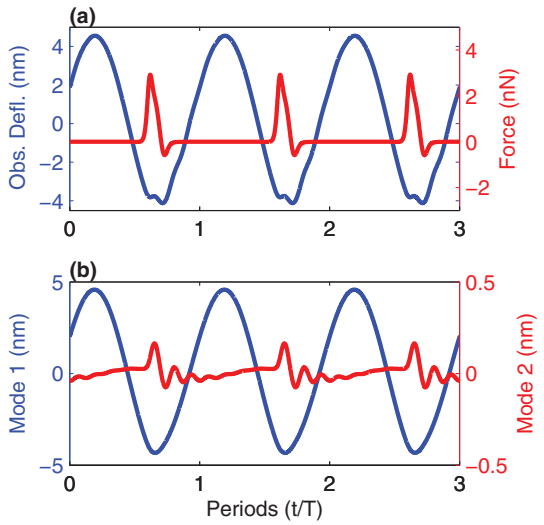

FIG. 6. (Color online) Time history of the simulation of Figure 5 at a setpoint ratio of 70%. (a) The observed deflection is approximately sinusoidal but there is a significant distortion when the tip taps on the sample (i.e., when the tip-sample force is high). (b) Examination of the individual eigenmode responses shows the distorted deflection waveform represents a significant amount of energy transferred into the second eigenmode.

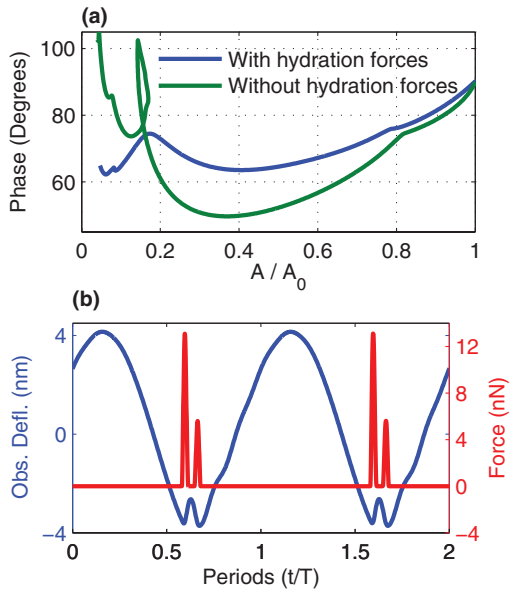

FIG. 7. (Color online) The effect of the hydration forces on the simulation of Figure 5. When the simulation is repeated without hydration forces (i.e., Hertz only) there is a significant change in the phase response (a). The time history of response at 70% setpoint without hydration force (b) shows two separate taps on the samples, as compared to Figure 6 with hydration forces, which showed only a single tap.

three times per drive cycle). However, based the time history (not shown), the tip is only tapping on the sample once per drive cycle in the vicinity of this peak. The resolution of this discrepancy is that Ref. 13 considered only a Hertz model and did not include the hydration forces. The hydration forces serve to smooth/damp out the non-linear behavior, so the multiple impact condition reported by Ref. 13 does not occur. To illustrate the effects of the hydration force, we show a second simulation in Figure 7. When the hydration force is removed, the phase is affected across all setpoints, and in particular the peak near 16% setpoint is now multi-valued with respect to amplitude. Further, comparing time histories (Figures 7(b) and 6(a)), it can be seen that in the pure Hertz model, the tip is tapping on the sample twice per drive cycle, but with the hydration forces, the tip is tapping only once. The hydration forces thus have a large effect on the response, despite the fact that the unconstrained amplitude is more than 20 times larger than the decay length of the hydration force.

B. Non-linear frequency response in air

A new tool in VEDA 2.0 is a frequency sweep tool. This can be useful for modeling and understanding the frequency dependence of various excitation methods (especially for FM-AFM in liquids[56]). It is also useful for understanding the cantilever's non-linear frequency response when interacting with the sample.

In this section, we will recreate the results of Ref. 5 using VEDA. Ref. 5 studied the dynamics of a relatively soft (0.87 N/m) cantilever interacting with an HOPG surface in dry nitrogen. Both experiments and analytical continuation software (AUTO97 (Ref. 71)) were used.

TABLE III. Parameters used for the simulation in Figure 8 (nonlinear frequency response).

Simulation	Frequency sweep
Unconstrained amplitude (nm)	89.2
Cantilever stiffness (N/m)	0.87
Quality factor	33.3
Natural frequency (kHz)	44
Sweep time (s)	0.2
Z separation (nm)	90
Tip-sample interaction model	DMT
Intermolecular distance (nm)	0.38
Hamaker constant (J)	2.96e-19
Young's Modulus of sample	10

Before presenting the results, we note two differences between VEDA and AUTO. First, the DMT contact model (3) is non-smooth at $d = a_0$. This presents a problem for AUTO, so Ref. 5 has artificially smoothed the interaction model. Non-smooth models do not present a problem for VEDA as the ODE solver used (DDASKR (Ref. 33)) performs well on non-smooth systems. Second, AUTO is able to find unstable branches (the dashed lines in Figure 9 of Ref. 5). VEDA integrates the differential equation numerically and so only the stable branches can be plotted.

The parameters are given in Table III. A series of 11 simulations is run for unconstrained amplitudes ranging from 89.2 nm to 90.2 nm in 0.1 nm steps.[72]

The result is shown in Figure 8. The lowest curve, representing $A_0 = 89.2$ nm, is approximately the frequency response of a linear single degree of freedom oscillator. The distance of closest approach (the minimum gap) is 0.8 nm. At this range the van der Waals forces are almost zero, so there is little non-linear effect. With each successive curve, the minimum gap decreases, so van der Waals forces start to be significant. On each curve, the point at which the phase is 90 degrees (the effective natural frequency) is indicated with a dot. For the first few simulations, these points are decreasing in frequency as amplitude increases. This is characteristic of a softening non-linearity.[73] Then, as the amplitude increases further, the natural frequency will start to increase. This indicates that the repulsive DMT forces are starting to exert a stiffening effect. Connecting the natural frequency points for each curve creates the "backbone" curve of the non-linear resonance, shown as a dashed line on the plot.

Figure 8(b) shows the mean interaction forces. As A_0 increases, the mean forces become more and more negative (attractive) until $A_0 = 89.8$ nm. At 89.8 nm the mean force is still attractive but it is has started to turn around and come back towards zero. At $A_0 = 90.0$ the mean force has become positive (repulsive) for the first time. This is the transition between the so-called attractive and repulsive imaging regimes.

In an experiment, the tip-sample interaction force could not be observed directly. But the cantilever phase can be observed, as shown in Figure 8(c). In the attractive regime, the phase angle increases (relative to the linear case) as the frequency sweeps through resonance but in the repulsive regime, the phase angle decreases.[5,74]

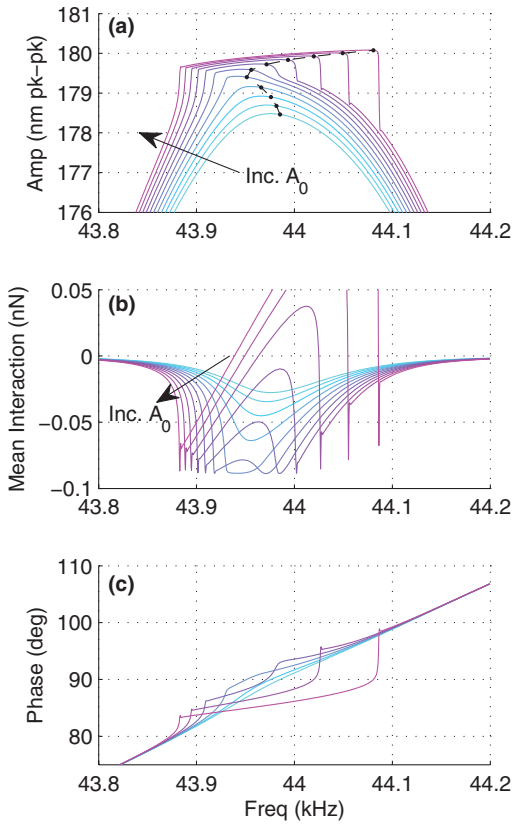

FIG. 8. (Color online) Non-linear frequency response for a cantilever in dry nitrogen near a surface modeled with DMT contact for a series of increasing amplitudes. The first simulation is for $A_0 = 89.2$ nm and each successive simulation increases A_0 by 0.1 nm. (a) First harmonic amplitude. As the amplitude is increased, the backbone curve (dashed line) moves left due to the softening effect of the van der Waals forces and then right due to the stiffening effect of the repulsive contact forces. (b) Mean interaction forces. (c) First harmonic phase lag (for clarity, only every other simulation is shown).

C. Frequency modulation force spectroscopy in vacuum

Another new capability in VEDA 2.0 is frequency modulation. In this example, we reproduce the simulation of Ref. 60, the approach of a silicon tip onto a (111) silicon facet. The parameters are shown in Table IV.

TABLE IV. Parameters for the simulation of Figure 9 (FM in vacuum).

Simulation	FM approach curves
Unconstrained amplitude (nm)	7
Cantilever stiffness (N/m)	30
Quality factor	30,000
Natural frequency (kHz)	150
Lock-in bandwidth (kHz)	20
Lock-in order	4th
Approach velocity (nm/s)	2
Tip Radius (nm)	5
Hamaker constant (J)	1.865e-19
Equilibrium position (nm)	0.2357
Range (nm)	0.12
Depth (J)	3.641e-19

TABLE V. Parameters used in the simulations of Figure 10 (electrostatic force microscopy). The bottom set of parameters is used only in the second simulation.

Simulation	AM approach curves
Unconstrained amplitude (nm)	1
Cantilever stiffness (N/m)	1
Quality factor	100,150
Natural frequency (kHz)	10,62
Driving frequency (kHz)	10
Lock-in bandwidth (kHz)	0.2
Approach velocity (nm/s)	20
Dielectric constant	80
DC Bias (V)	1
AC Bias (V)	1
Cantilever length (um)	100
Cantilever width (um)	25
Cantilever angle (deg)	10
Tip height (um)	20
Tip cone angle (deg)	20

The first curve to check in a FM-AFM approach curve is the controller performance. The first harmonic amplitude and first harmonic phase versus minimum gap (distance of closest approach) are shown in Figures 9(a) and 9(b). Ideally, these curves would be perfectly flat, but in a real system there is always some deviation. In this case, the phase is constant to within about 0.01 degree during the majority of the approach and starts to deviate slightly at the very end (where the Morse potential starts changing very rapidly). The oscillations in the phase could be reduced further by reducing the bandwidth of the lock-in amplifier, however that would also

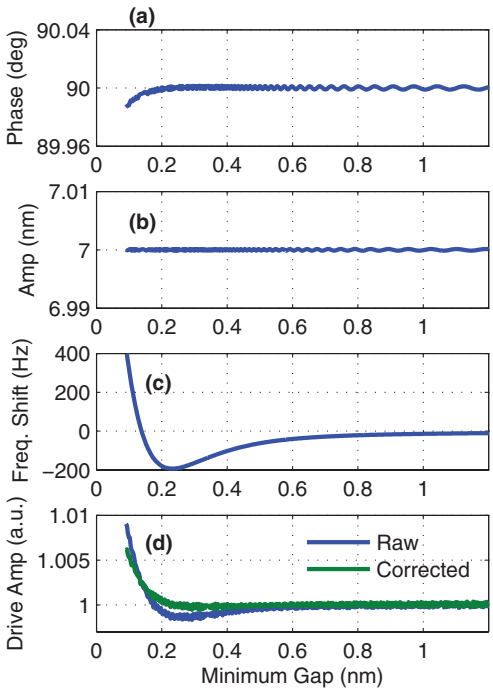

FIG. 9. (Color online) Simulation of FM-AFM approach to a Si surface in ultra-high vacuum. (a) Phase (lag), (b) amplitude, (c) frequency shift, and (d) drive amplitude ("dissipation").

increase the phase deviation at the very end. The amplitude controller also performs well, less than 0.002% deviation over the entire range. This controller performance would be considered acceptable.

Figure 9(c) shows the frequency shift versus minimum gap (also known as the "distance of closest approach"). The shape of the frequency shift follows the tip-sample interaction force. In fact, the exact tip-sample interaction force should be recoverable from the frequency shift.[75]

Figure 9(d) shows the drive amplitude, which is sometimes called the "dissipation." The drive amplitude increasing by about 0.9% over the approach. But, the Morse potential is a purely conservative interaction, so there is no actual tip-sample dissipation. Therefore, this 0.9% increase is entirely an instrumental artifact. Identifying precisely the cause of these instrumental artifacts was a major focus of Ref. 60. Indeed, they modeled a particular instrument in great detail in order to make detailed comparisons between simulation and experiment as to the exact amount of apparent versus true dissipation. In our case, we have not modeled a specific instrument, but a generic one. We can still make some generic comments as to the cause of apparent dissipation in this case. First, we note in Figure 9(c) that the drive frequency has increased by 0.27% over the approach. But the energy dissipated by a simple harmonic oscillation is dependent on the frequency,[76] therefore we should expect that the drive amplitude should increase by the same 0.27% solely due to this shift in drive frequency.[56] We can remove this effect by multiplying the drive amplitude by ω_0/ω. When this is removed, the corrected drive amplitude shows an increase of 0.6% over the approach. This corrected drive amplitude starts to deviate from unity at approximately the same minimum gap as the phase starts to deviate from 90 degrees. The phase error indicates that the natural frequency is changing too quickly for the PLL to keep up and thus the drive frequency is no longer tracking the natural frequency. Because the cantilever is driven off resonance, more energy is required for the same amplitude. To reduce the phase error, one would need to slow down the Z approach speed in order to allow the PLL more time to respond.

D. Higher eigenmode resonant enhancement of electrostatic force microscopy

Electrostatic Force Microscopy is a variant of AFM which attempts to measure electrostatic forces between an electrically conductive tip and a sample. This is typically a multi-frequency method. A mechanical vibration applied at one frequency is used for tip-sample sample distance control. An electrical bias applied at another frequency creates an electrostatic force at that frequency, which in turn creates a mechanical vibration that can be detected to measure the electrostatic force. The two different frequencies can be combined with AM and FM detection in multiple different ways.[77] In this section, we show a simulation which uses AM detection at both frequencies.

We demonstrate one of the ideas of Ref. 78. Two simulations using the sphere-plane model[22] are shown in Figure 10(a). Parameters are given in Table V. In the first simulation, the cantilever is excited mechanically at the first natural frequency ($\omega_d = \omega_1$) and electrically below the first natural frequency ($\omega_{AC} = 0.4\omega_1$). Then a lock-in amplifier is used to extract the motion at $0.4\omega_1$. There is a response present, but it is small. In the second simulation, the AC frequency is tuned to the cantilever's 2nd natural frequency $\omega_{AC} = \omega_2 \approx 6.2\omega_1$ thus exciting the second bending eigenmode. The electrostatic force exerted on the cantilever is exactly the same as in the first case. However, due to resonant amplification (and increased optical lever sensitivity at the second eigenmode, equation (13)) the response is more than 10 times larger. This improved sensitivity means that smaller electrostatic forces could be probed. For example, small differences in contact potential between two areas of a sample could be resolved better.

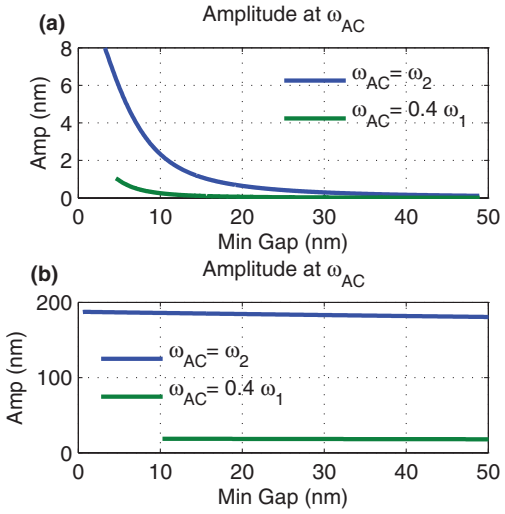

FIG. 10. (Color online) Detection of electrostatic force using an AC bias voltage at two different frequencies. When the bias is tuned to the frequency of the cantilever's second eigenmode, the force sensitivity is enhanced due to resonant amplification. (a) Using the sphere-plane model (Ref. 22). (b) Using a full cantilever model (Ref. 23).

In Figure 10(b) the same simulation is repeated, but this time using the full cantilever model.[23] The response amplitudes are significantly higher as compared to Figure 10(a). This is because the electrostatic forces due to the 100 × 25 μm cantilever body are included, in addition to the 10 nm radius tip. Also, in Figure 10(a) there is a significant increase in the response amplitude as the tip approaches the sample, whereas in Figure 10(b) the force appears nearly constant. This is because the cantilever body is the dominant contributor to the forces. The cantilever body is offset from the sample by the 20 μm tip height. Compared to the tip height, a change in Z distance of 50 nm is only 0.25%, so the electrostatic forces from the cantilever body are essentially constant. It is only the forces from the tip that change significantly as the cantilever approaches the sample, but these are only a small portion of the total response. This shows the importance of using realistic electrostatic models, and demonstrates one reason why obtaining high lateral resolution may be challenging in electrostatic force microscopy.

E. Material contrast in bimodal scanning

The term bimodal refers to exciting multiple eigenmodes simultaneously. This typically used to increase lateral

TABLE VI. Parameters used in the simulation of Figures 11 and 12 (bimodal).

Simulation	AM scanning
Unconstrained amplitude (nm)	14, 1.1
Cantilever stiffness (N/m)	10, 400
Quality factor	298, 752
Natural frequency (kHz)	106, 667
Drive frequency (kHz)	106,667
Tip mass	0
Setpoint ratio	0.9
Proportional gain	0.04
Integral gain	0.003
Lines/s	0.5
Intermolecular distance	0.1
Hamaker constant (J)	6.7e-20, 4.5e-20

resolution or enhance material contrast.[39,79,80] In this example, we demonstrate the use of AM-AFM bimodal scanning over a heterogeneous sample.

In traditional tapping mode AM, the 1st harmonic phase provides information on material properties. Its interpretation, however, is often misunderstood. Specifically, tapping mode gives information on the *ratio* of dissipative to conservative properties. An important implication is that if the dissipation is zero, then this ratio is always zero, regardless of the conservative properties. Bimodal AM-AFM on the other hand, is able to provide information on conservative properties even if the dissipation is zero.

In this example, we simulate the experimental results of Ref. 81 who considered regions of Sexithienyl (T6) deposited on a silicon substrate. The simulation parameters are given in Table VI and are taken from Ref. 81. The operating conditions are such that the cantilever is operated in a non-contact attractive regime. Thus, observed contrast between the silicon and T6 will be due entirely to differences in the attractive forces, and energy dissipation is expected to be very small.

The simulation consists of a bimodal scan over a substrate of length 30 nm that has a trapezoidal feature on it (Figure 11(a)). The substrate (Si) has a Hamaker constant of 6.7×10^{-20} J and the feature (T6) has a Hamaker constant of 4.5×10^{-20} J. Importantly, the tip-sample interaction is purely conservative—there is no energy dissipation. The result is shown in Figure 11. For comparison, a conventional single mode scan is also simulated. In Figure 11(b), the measured topography is shown. The feature extends from X = 10 nm to X = 20 nm. In Figure 11(c) the first frequency phase is shown. There is essentially no contrast between the two different regions in either the bimodal or conventional operation. However, the second frequency phase, which is a new signal available in bimodal that does not exist in conventional tapping mode shows a clear contrast to the Hamaker constant of the sample.

Although VEDA reports averaged quantities such as amplitude and phase by default (as in a real AFM), it can also output the raw time histories of tip-sample force and cantilever deflection. Such a plot is shown in Figure 12. In this

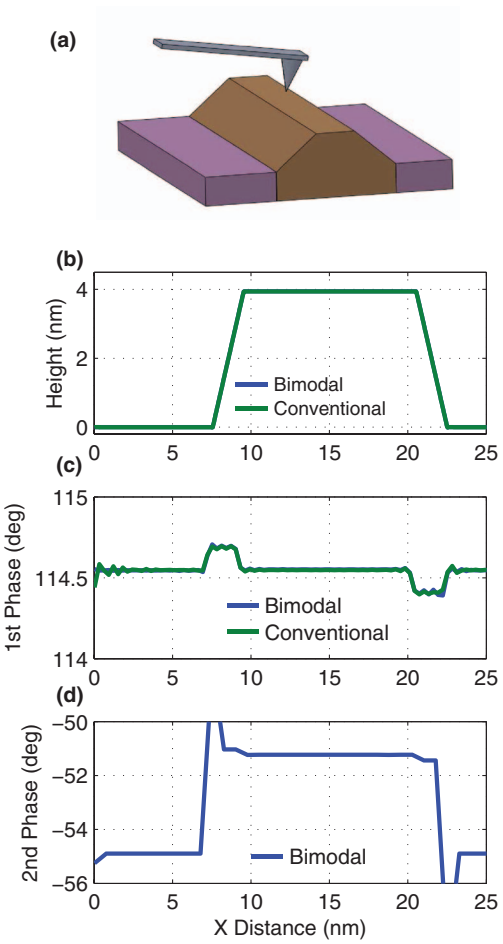

FIG. 11. (Color online) Simulation of a bimodal scan over a heterogeneous sample. (a) Schematic of sample showing different region. The substrate and trapezoidal feature have different Hamaker constants. (b) Measured topography. (c) Phase (lag) at the first drive frequency. (d) Phase (lag) at the second drive frequency.

case, the smaller second eigenmode excitation is clearly seen on top of the large first eigenmode response. An important point is that the interaction is not the same on every tap. This is because the ratio of drive frequencies is not an integer. For this case, the interaction will repeat every 5 periods of the 1st eigenmode.

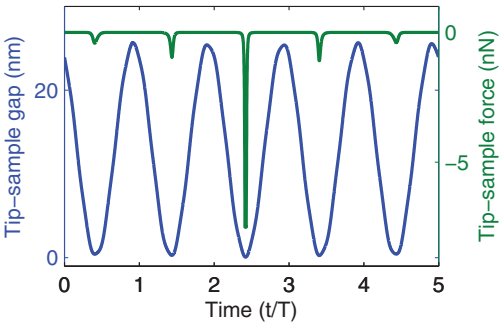

FIG. 12. (Color online) Time history of tip-sample gap and tip-sample force for the simulation of Figure 11 at X = 15 nm.

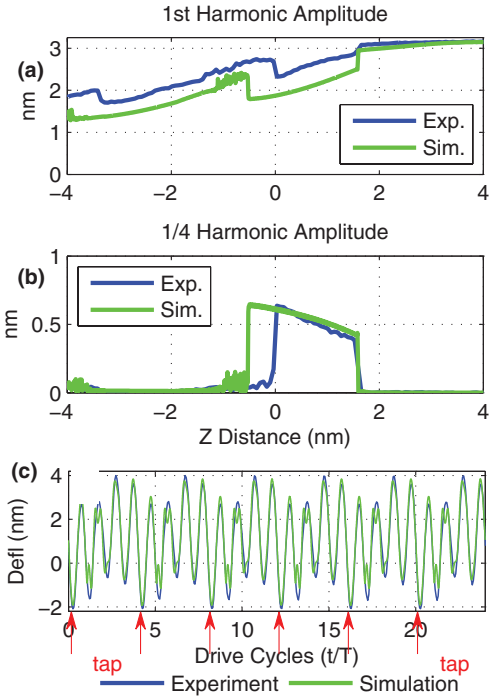

FIG. 13. (Color online) Subharmonic response when operating at the second cantilever eigenmode in liquids. (a) The first harmonic amplitude shows unexpected jumps. Those jumps correspond exactly to jumps in the 1/4 harmonic amplitude (b), indicating the onset of a period-4 response (i.e., a response at 1/4 the drive frequency). This is best understood in a time history (c) which shows that in this regime the cantilever taps on the sample only once every four drive cycles.

F. Subharmonic response when operating at higher eigenmodes

In this example, we examine the results of Ref. 82, in which multiple frequencies respond in liquids even when the excitation is single frequency. In that work, an excitation was applied at a cantilever's second natural frequency in water. An example approach curve on mica is shown in Figure 13(a). There are some interesting jumps up and down in the amplitude. These correspond to region in which there is a subharmonic response. That is, the cantilever is responding at a lower frequency than the driving frequency. For example, in Figure 13(b), there is a region where the cantilever responds at one-fourth of the driving frequency. This response is perhaps best understood in terms of a time history plot, such as Figure 13(c). When the cantilever taps on the sample, a significant amount of energy is transferred from the driving frequency to the first eigenmode. The low frequency response of the first eigenmode causes the tip to move so far away from the sample, that it does not tap on the next drive cycle. In fact, the tip taps only once every four drive cycles. Depending on the cantilever parameters and operating conditions, two, three, or even five drive cycle patterns are possible.

The comparison between simulation and experiment in Figure 13 is excellent (parameters given in Table VII). There are two points that are important in capturing this behavior. First, although the qualitative behavior can be reproduced fairly well by modeling only the first eigenmode, a quantitative match requires the use of three eigenmodes.

TABLE VII. Parameters for the simulation of Figure 13 (subharmonic response).

Simulation	AM approach curves
Natural frequency (kHz)	10, 76, 212
Driving frequency (kHz)	76
Modal stiffness (N/m)	0.6, 23.6, 185
Unconstrained amplitude (nm)	3.1
Quality factor ($\frac{1}{2\zeta}$)	2.8, 6.5, 9
Sample Young's modulus (GPa)	60
Approach speed	20 nm/s
Lock-in bandwidth	2 kHz
Hydration force decay length (nm)	0.245
Hydration force scaling	5e6
Noncons. hydration force decay length (nm)	0.245
Noncons. hydration force scaling (kg/s)	1e-5

This represents that fact that when the tip taps, energy is transferred from the driving harmonic to both lower and higher frequencies. Second, in Ref. 82 a qualitative match between experiment and simulation was achieved using a plain Hertz model. An improved quantitative match is achieved in this work by including solvation/hydration forces. For the conservative portion of the force, the same value from Sec. IV A is used. For the non-conservative force, the value from Sec. IV A did not give a good result. Instead a different value was fit to match these results.

G. Scanning artifacts due to jump to contact instability

In this example we demonstrate an imaging artifact that can occur on sticky (i.e., highly adhesive) samples, and can also be caused by the tip picking up debris from the sample. An experimental image demonstrating this artifact is shown in Figure 14(a). A TR400 cantilever (Olympus) is used to image a flat gelatin substrate in a phosphate buffer solution (commonly used for imaging biological samples such as cells), in an Asylum MFD3D. The top half of the image, which used a higher setpoint, reproduces the topography accurately, but the bottom half, which used a lower setpoint, does not. Examination of the topgraphy and amplitude cross sections (Figures 14(b) and 14(c)) shows that for the unstable situation, the repeated series of triangular features in topography is accompanied by negative spikes in the amplitude.

Instead of switching setpoints during a simulation, we recreate this instability in slightly different way. We consider a completely flat sample modeled by Hertz contact and the hysteretic adhesive force given in Sec. II A 7. The sample is split into two regions, the first part having a small adhesion force and the second part having much larger adhesion force. We expect the controller to be stable in the region of small adhesion and unstable in the region of large adhesion. The parameters are given in Table VIII.

The measured topography output for an unconstrained amplitude $A_0 = 6$ nm is shown in Figure 15(a). On the region with higher adhesion (to the right of X = 25), there is a series of sharp spikes, precisely as observed experimen-

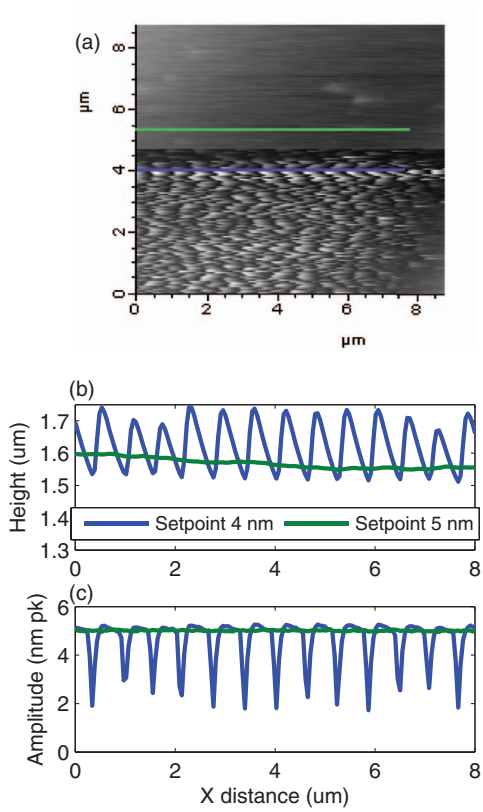

FIG. 14. (Color online) Experimentally observed jump-to-contact instability. (a) Topography image of a flat gelatin substrate in phosphate buffer solution. In the lower half of the image, the controller is unstable. The cantilever repeatedly sticks to and pulls away from the substrate. In the upper half of the image, the controller setpoint was raised, removing the instability. Also shown are cross sections of (b) topography and (c) amplitude in the two different regions.

tally. The cantilever is alternatively approaching and then retracting from the surface and never finds any stable imaging condition.

In order to understand this instability, we examine the approach curve for this cantilever on the high adhesion sample. This result is shown in Figure 15(b). The cantilever snaps in to permanent contact with the surface at a very high setpoint. This explains the scanning behavior. The cantilever starts far from the surface with a large amplitude. The

TABLE VIII. Parameters for the simulation of Figure 15 (controller instabilities).

Simulation	AM scanning
Natural frequency (kHz)	40, 251
Driving frequency (kHz)	40
Modal stiffness (N/m)	1, 39.3
Unconstrained amplitude (nm)	6
Quality factor ($\frac{1}{2\zeta}$)	10, 12
Setpoint	0.6
Sample Young's Modulus (GPa)	1
Critical gap (nm)	0.3
Energy dissipated (eV)	$\begin{cases} 1, & X < 25 \\ 10, & X > 25 \end{cases}$
Lock-in bandwidth	1 kHz

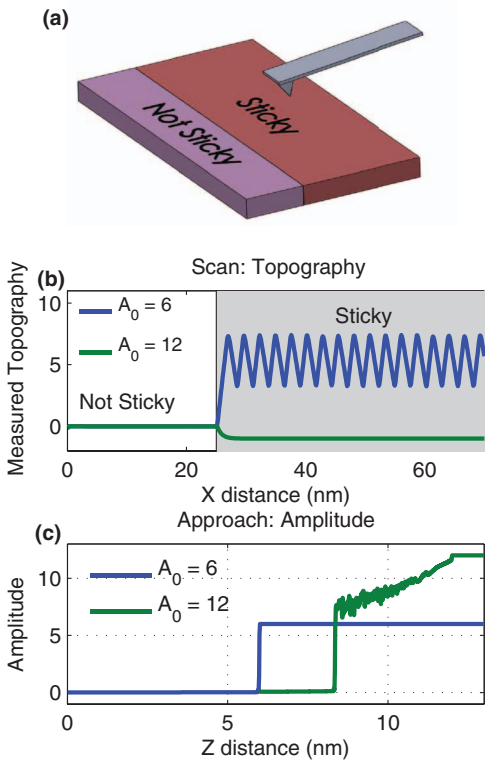

FIG. 15. (Color online) Controller instabilities in liquid on sticky samples. (a) Schematic. The sample is flat, but has regions of different material properties: one region is sticky and other is not. (b) Topography for two simulated scans. For a small free amplitude, the controller is unstable in the sticky region, first approaching and then retracting from the sample. For a larger free amplitude, the controller is stable. (c) Dynamic approach curves on the sticky region explain the cause of the instability. For the small free amplitude, the cantilever jumps to contact as soon as it touches the sample. Therefore, there is no Z distance at which a scanning setpoint of 60% exists. For the larger free amplitude, the jump-to-contact point does not happen until a lower setpoint.

controller brings the cantilever closer to the surface to reduce the amplitude. However, before the amplitude is reduced to the setpoint of 60%, the cantilever snaps-in and the amplitude jumps to nearly 0. The controller sees that this amplitude reduction has gone too far, and pulls the cantilever away from the sample in order to increase the amplitude. At that point, the cantilever pulls off the sample and obtains a large amplitude again. The process then repeats.

For this set of simulation parameters, there are no controller gains, scanning speeds, or setpoints that would make this system stable. The only choice is to change the free amplitude. We expect that raising the free amplitude should help reduce the instability. In fact, increasing A_0 to 12 nm does make the scan more stable as shown in Figure 15(a), and this is reflected in the approach curves Figure 15(b) as well.

V. SUMMARY AND OUTLOOK

In summary, we have described some of the new features available in VEDA 2.0, focusing specifically on cantilever dynamics, new materials modeling, and new controller/instrumentation modeling. In particular we have highlighted the multi-modal cantilever dynamics and solvation forces models needed to accurately simulate liquid environments. The new version includes a complete set of

simulations for many different types of AFM experiments including many that space did not permit discussing (e.g., force-distance curves, FM scanning, and JKR contact model). The simulator is useful for providing insight into complex behavior, running studies to determine the sensitivity of the observables to various parameters, and teaching new students the fundamentals of AFM.

New tip-sample interaction models in development include: electrostatic models that take non-conservative interactions into account, enhanced viscoelasticity models, additional hysteretic models, and the ability to link tip-sample interactions from molecular dynamics simulations directly into VEDA.

We believe there is a compelling case to be made for web-based simulations for the AFM community. In addition to simulations, we plan to add the ability for users to upload experimental data for online analysis such as fitting force distance curves to models or extracting elasticity data from images. Such a central resource will help standardize analyses across the AFM community and allow researchers to access state-of-the-art data processing without needing to write their own codes.

ACKNOWLEDGMENTS

We thank Steven Johnson for assistance with the FORTRAN coding, Hank Thompson for assistance with the electrostatic forces, Tridib Saha and Alex Cartagena for assistance with Figure 14, as well as Professor Ron Reifenberger, Professor Joel Chevrier, Roger Proksch (Asylum Research), Greg Meyers (Dow Chemical), and many other VEDA users for feedback and suggestions on previous versions of VEDA. Financial support was provided in part by Dow Chemical corporation, the Network for Computational Nanotechnology and the National Science Foundation through Grant Nos. 0700289 and CMMI-0927648.

[1] Y. Martin, C. C. Williams, and H. K. Wickramasinghe, J. Appl. Phys. **61**, 4723 (1987).
[2] B. Anczykowski, D. Krüger, and H. Fuchs, Phys. Rev. B **53**, 15485 (1996).
[3] R. García and A. S. Paulo, Phys. Rev. B **60**, 4961 (1999).
[4] J. Berg and G. A. D. Briggs, Phys. Rev. B **55**, 14899 (1997).
[5] S. I. Lee, S. W. Howell, A. Raman, and R. Reifenberger, Phys. Rev. B **66**, 115409 (2002).
[6] U. Schwarz, H. Haefke, P. Reimann, and H. Güntherodt, J. Microscopy **173**, 183 (1994).
[7] A. L. Weisenhorn, P. K. Hansma, T. R. Albrecht, and C. F. Quate, Appl. Phys. Lett. **54**, 2651 (1989).
[8] S. Jarvis, A. Oral, T. Weihs, and J. B. Pethica, Rev. Sci. Instrum. **64**, 3515 (1993).
[9] G. Schitter, F. Allgöwer, and A. Stemmer, Nanotechnology **15**, 108 (2004).
[10] J. E. Sader, J. Appl. Phys. **84**, 64 (1998).
[11] J. Melcher, S. Hu, and A. Raman, Rev. Sci. Instrum. **79**, 061301 (2008).
[12] D. Martínez-Martín, C. Carrasco, R. Pérez, M. Mateu, J. Carrascosa, P. de Pablo, J. Gómez-Herrero, D. Kiracofe, J. Melcher, and A. Raman, "Resolving mechanical properties at the nanoscale in viruses with frequency modulation atomic force microscopy," PLoS One (in press).
[13] J. Melcher, X. Xu, and A. Raman, Appl. Phys. Lett. **93**, 093111 (2008).
[14] J. Melcher, C. Carrasco, X. Xu, J. L. Carrascosa, J. Gómez-Herrero, P. J. D. Pablo, and A. Raman, Proc. Natl. Acad. Sci. U.S.A. **106**, 13655 (2009).
[15] See https://nanohub.org/tools/adac to run VEDA, as well as to access the online manual.
[16] K. L. Johnson, *Contact Mechanics* (Cambridge University Press, Cambridge, UK, 1985).
[17] R. S. Chadwick, SIAM J. Appl. Math. **62**, 1520 (2002).
[18] B. V. Derjaguin, V. M. Muller, and Y. P. Toporov, J. Colloid Interface Sci. **53**, 314 (1975).
[19] K. L. Johnson, K. Kendall, and A. Roberts, Proc. R. Soc. London Ser. A **321**, 301 (1971).
[20] P. Morse, Phys. Rev. **34**, 57 (1929).
[21] J. Lennard-Jones, Proc. R. Soc. London Ser. A **106**, 463 (1924).
[22] L. Xu and M. Salmeron, "Studies of wetting and capillary phenomena at nanometer scale with scanning polarization force microscopy," *Nano-Surface Chemistry* (Marcel Dekker, New York, 2001), Chap. VI, pp. 243–287.
[23] A. Gil, J. Colchero, J. Gómez-Herrero, and A. Baro, Nanotechnology **14**, 332 (2003).
[24] T. C. T. Ting, J. Appl. Mech. **33**, 845 (1966).
[25] M. Kober, E. Sahagun, M. Fuss, F. Briones, M. Luna, and J. J. Saenz, Phys. Status Solidi (RRL) **2**, 138 (2008).
[26] H. Butt, K. Graf, M. Kappl, and J. Wiley, *Physics and Chemistry of Interfaces* (Wiley-VCH, Berlin, 2003).
[27] J. Israelachvili, *Intermolecular and Surface Forces*, 2nd Ed. (Academic, New York, 1992).
[28] S. Jeffery, P. M. Hoffmann, J. B. Pethica, C. Ramanujan, H. O. Özer, and A. Oral, Phys. Rev. B **70**, 054114 (2004).
[29] G. B. Kaggwa, J. I. Kilpatrick, J. E. Sader, and S. P. Jarvis, Appl. Phys. Lett. **93**, 011909 (2008).
[30] S. deBeer, D. Ende, and F. Mugele, Nanotechnology **21**, 325703 (2010).
[31] Assuming that the radius of curvature of the sphere is larger than the contact radius and that the plane can be approximated as a half-space.
[32] H. Dankowicz and M. Paul, J. Comput. Nonlinear Dyn. **4**, 041009 (2009).
[33] P. N. Brown, A. C. Hindmarsh, and L. R. Petzold, SIAM J. Sci. Comput. (USA) **15**, 1467 (1994).
[34] H. Hölscher, A. Schwarz, W. Allers, U. D. Schwarz, and R. Wiesendanger, Phys. Rev. B **61**, 12678 (2000).
[35] G. Lee, D. Kidwell, and R. Colton, Langmuir **10**, 354 (1994).
[36] P. Hinterdorfer, W. Baumgartner, H. Gruber, K. Schilcher, and H. Schindler, Proc. Natl. Acad. Sci. U.S.A. **93**, 3477 (1996).
[37] T. R. Rodríguez and R. García, Appl. Phys. Lett. **80**, 1646 (2002).
[38] S. Basak and A. Raman, Appl. Phys. Lett. **91**, 064107 (2007).
[39] T. R. Rodríguez and R. García, Appl. Phys. Lett. **84**, 449 (2004).
[40] O. Sahin, G. Yaralioglu, R. Grow, S. Zappe, A. Atalar, C. Quate, and O. Solgaard, Sens. Actuators, A **114**, 183 (2004).
[41] R. C. Tung, A. Jana, and A. Raman, J. Appl. Phys. **104**, 114905 (2008).
[42] D. Kiracofe and A. Raman, J. Appl. Phys. **107**, 3506 (2010).
[43] L. Meirovitch, *Principles and Techniques of Vibrations* (Prentice Hall, Englewood Cliffs, NJ, 1997).
[44] J. Melcher, S. Hu, and A. Raman, Appl. Phys. Lett. **91**, 53101 (2007).
[45] G. Meyer and N. M. Amer, Appl. Phys. Lett. **53**, 1045 (1988).
[46] D. Walters, J. Cleveland, N. Thomson, P. Hansma, M. Wendman, G. Gurley, and V. Elings, Rev. Sci. Instrum. **67**, 3583 (1996).
[47] M. Higgins, R. Proksch, J. Sader, M. Polcik, S. Mc Endoo, J. Cleveland, and S. Jarvis, Rev. Sci. Instrum. **77**, 013701 (2006).
[48] A. Raman, R. Reifenberger, J. Melcher, and R. Tung, Cantilever dynamics and nonlinear effects in atomic force microscopy, in *Noncontact Atomic Force Microscopy* (Springer, Berlin/Heidelberg, 2009), Chap. 18.
[49] R. Stark, T. Drobek, and W. Heckl, Ultramicroscopy **86**, 207 (2001).
[50] O. D. Payton, L. Picco, A. R. Champneys, M. E. Homer, M. J. Miles, and A. Raman, Rev. Sci. Instrum. **82**, 043704 (2011).
[51] X. Xu and A. Raman, J. Appl. Phys. **102**, 034303 (2007).
[52] D. Kiracofe and A. Raman, Nanotechnology **22**, 485502 (2011).
[53] Phase modulated approach curves are also possible by setting the PLL gains to zero.
[54] J. I. Kilpatrick, A. Gannepalli, J. P. Cleveland, and S. P. Jarvis, Rev. Sci. Instrum. **80**, 23701 (2009).
[55] M. Kageshima, T. Chikamoto, T. Ogawa, Y. Hirata, T. Inoue, Y. Naitoh, Y. J. Li, and Y. Sugawara, Rev. Sci. Instrum. **80**, 023705 (2009).
[56] A. Labuda, K. Kobayashi, D. Kiracofe, K. Suzuki, P. Grütter, and H. Yamada, AIP Advances **1**, 022136 (2011).
[57] R. Proksch and S. V. Kalinin, Nanotechnology **21**, 455705 (2010).
[58] S. Belikov and S. Magonov, "Simulation of atomic force microscopy of molecular structures and interplay with experiment," in *American Control Conference (ACC), 2010*, (IEEE, Baltimore, MD, 2010), pp. 5745–5750.
[59] J. Polesel-Maris and S. Gauthier, J. Appl. Phys. **97**, 044902 (2005).
[60] L. Nony, A. Baratoff, D. Schaer, O. Pfeiffer, A. Wezel, and E. Meyer, Phys. Rev. B **74**, 235439 (2006).
[61] G. Couturier, J. Aimé, J. Salardenne, and R. Boisgard, Eur. Phys. J. Appl. Phys. **15**, 141 (2001).

[62]M. Tsukada and N. Watanabe, Jpn. J. Appl. Phys. **48**, 5001 (2009).
[63]H. Pishkenari and A. Meghdari, Ultramicroscopy **111**, 107 (2011).
[64]G. Varadhan, W. Robinett, D. Erie, and R. M. Taylor II, Proc. SPIE **4665**, 16 (2002).
[65]Phase modulation is available by setting PLL controller gains to zero in FM.
[66]See http://www.rappture.org for information about the rappture toolkit.
[67]R. Reifenberger and A. Raman, "ME 597/PHYS 570: Fundamentals of Atomic Force Microscopy (Fall 2009)," http://nanohub.org/resources/7320.
[68]K. Voïtchovsky, J. Kuna, S. Contera, E. Tosatti, and F. Stellacci, Nat. Nanotechnol. **5**, 401 (2010).
[69]B. Anczykowski, B. Gotsmann, H. Fuchs, J. P. Cleveland, and V. B. Elings, Appl. Sur. Sci. **140**, 376 (1999).
[70]X. Xu, J. Melcher, S. Basak, R. Reifenberger, and A. Raman, Phys. Rev. Lett. **102**, 060801 (2009).
[71]E. J. Doedel, A. R. Champneys, T. F. Fairgrieve, Y. A. Kuznetsov, B. Sandstede, and X. J. Wang, "Auto97: Software for continuation and bifurcation problems in ordinary differential equations," Technical report, California Institute of Technology, Pasadena CA 91125, 1997.
[72]Reference 5 used a slightly different set of amplitudes.
[73]D. Jordan and P. Smith, *Nonlinear Ordinary Differential Equations: An Introduction to Dynamical Systems* (Oxford University Press, New York, 1999).
[74]S. Hu, "Nonlinear dynamics and force spectroscopy in dynamic atomic force microscopy," Ph.D. dissertation, Purdue University, 2007.
[75]J. E. Sader and S. P. Jarvis, Appl. Phys. Lett. **84**, 1801 (2004).
[76]J. P. Cleveland, B. Anczykowski, A. E. Schmid, and V. B. Elings, Appl. Phys. Lett. **72** (1998).
[77]M. Nakamura and H. Yamada, *Roadmap of Scanning Probe Microscopy* (Springer, New York, 2007), p. 43.
[78]A. Kikukawa, S. Hosaka, and R. Imura, Appl. Phys. Lett. **66**, 3510 (1995).
[79]S. Kawai, T. Glatzel, S. Koch, B. Such, A. Baratoff, and E. Meyer, Phys. Rev. Lett. **103**, 220801 (2009).
[80]N. F. Martínez, J. R. Lozano, E. T. Herruzo, F. García, C. Richter, T. Sulzbach, and R. García, Nanotechnology **19**, 384001 (2008).
[81]N. F. Martínez, S. Patil, J. R. Lozano, and R. García, Appl. Phys. Lett. **89**, 153115 (2006).
[82]D. Kiracofe and A. Raman, J. Appl. Phys. **108**, 034320 (2010).
[83]T. Senden and C. Drummond, Colloids Surf. **94**, 29 (1995).